

Lightning-Fast Thunderstorm Warnings: Predicting Severe Convective Environments with Global Neural Weather Models

Monika Feldmann^{*1}, Tom Beucler^{2,3}, Milton Gomez^{2,3}, and Olivia Martius¹

¹Institute of Geography - Oeschger Centre for Climate Change Research,
University of Bern

²Faculty of Geosciences and Environment, University of Lausanne

³Expertise Center for Climate Extremes, University of Lausanne

June 17, 2024

Abstract

The recently released suite of neural weather models can produce multi-day, medium-range forecasts within seconds, with a skill on par with state-of-the-art operational forecasts. Traditional neural model evaluation predominantly targets global scores on single levels. Specific prediction tasks, such as severe convective environments, require much more precision on a local scale and with the correct vertical gradients in between levels. With a focus on the convective season of global hotspots in 2020, we assess the skill of three top-performing neural weather models (Pangu-Weather, GraphCast, FourCastNet) for two variables used to assess convective activity (Convective Available Potential Energy - CAPE, and Deep Layer Shear - DLS) at lead-times of up to 10 days against the ERA-5 reanalysis and the IFS operational numerical weather prediction model. Looking at the example of a US tornado outbreak on April 12 and 13, 2020, all models predict elevated CAPE and DLS values multiple days in advance. The spatial structures in the neural weather models are smoothed in comparison to IFS and ERA-5. The models show differing biases in the prediction of CAPE values, with GraphCast capturing the value distribution the most accurately and FourCastNet showing a consistent underestimation. In seasonal analyses around the globe, we generally see the highest performance by GraphCast and Pangu-Weather, which match or even exceed the performance of IFS. CAPE derived from vertically coarse pressure levels of neural weather models nonetheless lacks the precision of CAPE derived from the vertically fine resolution of numerical models. The promising results here indicate that a direct prediction of CAPE in neural weather models is likely to be skillful. This would open unprecedented opportunities for fast and inexpensive predictions of severe weather phenomena. By advancing the assessment of large neural weather models towards process-based evaluations we lay the foundation for hazard-driven applications of artificial-intelligence-based weather forecasts.

*Corresponding author: monika.feldmann@unibe.ch

1 Introduction

AI(Artificial intelligence)-based deterministic forecasts are revolutionizing the landscape of medium-range weather forecasting (Ebert-Uphoff and Hilburn, 2023; Bouallègue et al., 2024). Among the models released in the past year are FourCastNet (Bonev et al., 2023), GraphCast (Lam et al., 2023) and Pangu-Weather (Bi et al., 2023). They are capable of forecasting the main atmospheric state variables on various pressure levels within seconds (on GPU, Wong, 2023), with a skill on par with the IFS model (Integrated Forecasting System, Bougeault et al., 2010, operational version of IFS) of the ECMWF (European Centre for Medium-range Weather Forecasts). AI-based weather predictions are rapidly revolutionizing weather forecasting (Bouallègue et al., 2024; Olivetti and Messori, 2024a; Beucler et al., 2024b; Brunet et al., 2023; Govett et al., 2024) with scientists and forecasting centers calling for action to scrutinize neural weather model performance from various perspectives, thereby going beyond simply verifying the atmospheric state (Ebert-Uphoff and Hilburn, 2023; Jeppesen, 2024; Bonavita, 2023). First studies investigate the robustness of forecasts for extremes (Charlton-Perez et al., 2024; Olivetti and Messori, 2024b) and model behavior in idealized experiments (Hakim and Masanam, 2024).

We here focus on the specific, application-oriented task of accurately predicting atmospheric profiles in convective environments. The skillful prediction of convective environments requires high accuracy in the vertical profile, as well as the simultaneous, correct prediction of both thermodynamic (temperature and humidity) and kinematic components (vertical wind shear). Convection requires atmospheric instability, which is governed by the vertical temperature and moisture profile (e.g., Houze, 2014; Trapp, 2013). Its severity is modulated by wind shear, emphasizing the importance of the wind profile (Houze, 2014; Trapp, 2013). By combining instability and wind shear, severe convective environments, that are related to particularly hazardous and impactful thunderstorms, can be identified (e.g., Taszarek et al., 2020; Kunz, 2007; Brooks et al., 2003).

Severe thunderstorms are among the most hazardous weather phenomena resulted in substantial losses worldwide in recent years (e.g., Bowen et al., 2024). Severe thunderstorms can produce large hail and severe wind gusts, along with torrential rain, lightning strikes, and tornadoes (Houze, 2014; Markowski and Richardson, 2010).

Current AI-based global forecasting at medium-range lead-times, provides weather information on 0.25° grid. These models can hence not explicitly forecast severe storms. For this reason, we focus here on the verification of pre-convective environments, which are characterized by the mesoscale patterns of instability and wind shear. These environments provide information on the propensity of the atmosphere to produce severe storms (e.g., Taszarek et al., 2021, 2020; Brooks, 2013) and are used for forecasting of severe convection (Battaglioli et al., 2023; Brooks et al., 2011; Kunz, 2007). Accurate and inexpensive forecasts of mesoscale convective environments enable the timely assessment of severe convective outlooks for hazardous weather warnings.

2 Data

We cannot use data for the verification that was used in the training of the AI-models (see Table 1), we therefore focus our analysis on the year 2020. We evaluate the three AI-models Pangu-Weather (Bi et al., 2023), GraphCast (Lam et al., 2023) and FourCastNet (Bonev et al., 2023). We focus on models with publicly accessible code and a stable version. Note that other AI-based global models have been developed (AIFS, FuXi, Aurora and ClimaX; Lang et al., 2024; Chen et al., 2023; Bodnar et al., 2024; Nguyen et al., 2023), but do not meet our evaluation requirements. The models are compared with the performance of IFS (Haiden et al., 2019,

IFS version of 2020). The reference model IFS is the operational, physics-based, numerical weather prediction model at ECMWF, used for global medium-range forecasts (Thepaut and Courtier, 1991; Bougeault et al., 2010). The ERA-5 reanalysis (Hersbach et al., 2020) serves as a ground truth. We obtain Pangu-Weather, GraphCast and IFS data through the benchmark dataset “Weatherbench2” (Rasp et al., 2024). FourCastNet forecasts are produced with the code-release of ECMWF (ECMWF, 2023).

To briefly summarize the architecture of the models, Pangu-Weather is a transformer model that uses a 3-D visual earth transformer to encode the relative location on a sphere and additionally employs a hierarchical temporal aggregation, combining a 24h-prediction model with a 6h-prediction model (Bi et al., 2023). GraphCast is a graph neural network, which is particularly useful for spatially structured data, and uses successive 6h-predictions (Lam et al., 2023). “FourCastNet v2 small” is a transformer model, employing spherical Fourier neural operators (SFNO) to account for the spatial encoding of a sphere (Bonev et al., 2023).

All data is gridded at a 0.25° resolution, IFS’ native 0.125° resolution is regridded using the MIR method (Meteorological Interpolation and Regridding, Barratt, 2017). The forecasts are available twice daily at 00h UTC and 12h UTC and available for up to 10 days lead-time in 6-hour increments. The AI-models are initialized from both ERA-5 and the IFS analysis. This reflects the conditions they were trained in (ERA-5) compared to an operational prediction set-up (IFS analysis). GraphCast has an additional operational version specifically tuned to being initialized with IFS data. IFS is initialized with the IFS analysis.

For the computation of convective parameters, we use the temperature, specific humidity (Q) and geopotential on the pressure levels listed in Table 1, as well as the horizontal wind on pressure levels (see Section 3.1). The models differ in the available pressure levels and in the moisture variable that they predict (specific and relative humidity - RH). A summary is provided in Table 1.

Model	Pressure levels	Moisture variable	Training period
IFS	50, 100, 150, 200, 250, 300, 400, 500, 600, 700, 850, 925, 1000	Q	
ERA5	50, 100, 150, 200, 250, 300, 400, 500, 600, 700, 850, 925, 1000	Q	
Pangu-Weather*	50, 100, 150, 200, 250, 300, 400, 500, 600, 700, 850, 925, 1000	Q	1979-2017
GraphCast*	1, 2, 3, 5, 7, 10, 20, 30, 50, 70, 100, 125, 150, 175, 200, 225, 250, 300, 350, 400, 450, 500, 550, 600, 650, 700, 750, 775, 800, 825, 850, 875, 900, 925, 950, 975, 1000	Q	1979-2017
GraphCast-oper*	50, 100, 150, 200, 250, 300, 400, 500, 600, 700, 850, 925, 1000	Q	1979-2017
FourCastNet*	50, 100, 150, 200, 250, 300, 400, 500, 600, 700, 850, 925, 1000	RH	1979-2015

Table 1: Model characteristics, neural weather models marked with an asterisk

3 Methods

3.1 Deriving convective parameters

We focus here on the convective parameters convective available potential energy (CAPE), deep-layer shear (DLS), and on a combined parameter of both called wmax-shear (WMS):

$$WMS = \sqrt{2 \cdot CAPE} \cdot DLS \quad (1)$$

CAPE is derived with the implementation found in WRF-python (Ladwig, 2017) and computes the most unstable CAPE. The parcel profile is launched at the level of the highest equivalent

potential temperature.

$$CAPE = g \cdot \int_{z_{LFC}}^{z_{LNB}} \frac{T'_v - T_v}{T_v} dz, \quad (2)$$

where T_v is the virtual temperature of the environment, T'_v the virtual temperature of the lifted parcel, g the gravity constant, z the altitude, LFC the level of free convection and LNB the level of neutral buoyancy. The relatively coarse vertical resolution reduces the accuracy of the CAPE calculation (Wang et al., 2021; Mensch, 2021). However, we apply the same procedure to all datasets, hence treating them equally. We thereby artificially reduce the number of vertical levels available in the IFS and ERA-5 data. If we use the full set of vertical levels from IFS the IFS CAPE is closer to observations from soundings than the CAPE calculated from the reduced set of pressure levels (not shown). To approximate the deep layer shear, we compute the magnitude of the differential wind vector between the surface and the 500 hPa level.

$$DLS = \sqrt{(u_{500} - u_{sfc})^2 + (v_{500} - v_{sfc})^2}, \quad (3)$$

where u and v are the horizontal components of wind at the surface and 500 hPa level.

3.2 Forecast evaluation

To evaluate the forecast quality, we use several different scores. We first compute the root mean square error (RMSE) and the bias, two standard scores. To account for displacement errors and avoid to so-called 'double penalty' (Gilleland et al., 2009; Gilleland, 2013), we additionally use the fractional skill score (FSS, Mittermaier, 2021) at different thresholds. The FSS identifies the area fraction of the target variable exceeding a used-defined threshold. We use an area with a radius of 1° in which the fraction exceeding the threshold is evaluated. A FSS value of 1 indicates a perfect forecast (see Table 2). Finally, we also use the structure, amplitude, and location (SAL) score, which evaluates these three properties individually (Wernli et al., 2008, 2009). A negative structure score indicates a too-fine spatial structure and too-small areas; a positive score indicates a too-large and too-flat distribution of values (smoothing). A low amplitude score indicates an underestimation, and a high score an overestimation. The location score accounts for both a mismatch in centroid, as well as a mismatch in overlap. A value of zero in each component indicates are perfect forecast (see Table 2).

Score	Value range	Optimal score
RMSE	≥ 0	0
BIAS	≤ 0	0
FSS	0,1	1
S	-2,2	0
A	-2,2	0
L	0,2	0

Table 2: Forecast evaluation metrics

We compute the FSS for two thresholds for each variable, describing the convective environment. The SAL score also identifies cohesive patches exceeding a given threshold. All thresholds for the scores and variables are summarized in Table 3. These thresholds are derived from Taszarek et al. (2017). While the thresholds also include environments with only a moderate likelihood of convective storm formation, they serve as an estimated lower bound on severe convective storm occurrence.

Variable	Unit	FSS thresholds	SAL threshold
CAPE	J kg^{-1}	300, 1000	300
WMS	$\text{m}^2 \text{s}^{-2}$	300, 500	300

Table 3: Variable thresholds for scores

4 Case Study: US tornado outbreak

4.1 Synoptic situation

Over the course of 12 and 13 April, 141 tornadoes were reported in 10 states, ranging up to a strength of EF4 (Storm Prediction Center, 2020a,b). With an estimated 450 Million \$ worth of property damage and 38 fatalities, this tornado outbreak was among the highest-impact events in the southern states (Beddoes, 2020), contributing to 2020 having the highest severe convective storm damages in the past (Bevere and Weigel, 2021).

The tornado outbreak was characterized by an anomalously warm period in the preceding month (Copernicus Services, 2020), leading to high sea surface temperatures in the Gulf of Mexico. The convective period was induced by a deep trough moving across the US. In the warm sector, warm and moist air from the Gulf was advected further north, over the Southeastern states. Simultaneously, the approaching trough was associated with high deep-layer wind shear, which is crucial for convective organization. The convective potential of the situation was well forecasted, the storm prediction center issued the first warnings four days before the convective outbreak (Dean and Dial, 2020).

While this event was most striking because of the large number of tornadoes, we focus here on the convective environment characterized by CAPE and DLS. Figure 1 shows the evolution of CAPE, DLS, the geopotential height anomaly, and the surface temperature anomaly during the outbreak.

The in-depth analysis of model forecast performance will focus on 13 April 2020 at 06:00 UTC. This is the environment a few hours before a elongated squall-line formed, which spawned the majority of the tornadoes.

4.2 Forecasting CAPE and DLS

We first want to investigate to which extent AI-models are capable of producing realistic CAPE and DLS values overall. For this purpose, we investigate a short lead-time of 30 hours. Fig. 2A) depicts CAPE and DLS in ERA-5 (Fig. 2a), the IFS forecast (Fig. 2b) and the forecast of the three AI-models Pangu-Weather (Fig. 2c), GraphCast (Fig. 2d) and FourCastNet (Fig. 2e). All models produce CAPE values in the right order of magnitude with a spatial distribution of DLS that corresponds well to the reference. Nonetheless we can see differences in between the models. All AI-model fields appear smoother than the reference data. IFS has the highest degree of spatial detail in both DLS and CAPE, while the AI-models mostly capture the larger-scale features. The high degree of detail in IFS, however, is penalized in the standard performance scores, as already a small displacement of features can lead to increases in RMSE (Fig. 2f), RMSE-IFS 330 J kg^{-1} , RMSE-GraphCast 283 J kg^{-1} ; for all scores see Table 5). FourCastNet underestimates CAPE in this case (Fig. 2i), while Pangu-Weather appears to overestimate CAPE in certain areas (Fig. 2g). Of the AI-models, GraphCast shows the closest match in terms of location and magnitude to ERA-5 (Fig. 2h).

We next take a look at the lead-time 174 hours (Fig. 2B), which corresponds to ~ 7 days. Once again, IFS has a high degree of spatial detail, whereas the AI-models are smooth. Their smoothness does not appear much more pronounced than in the 30-hour forecast which is

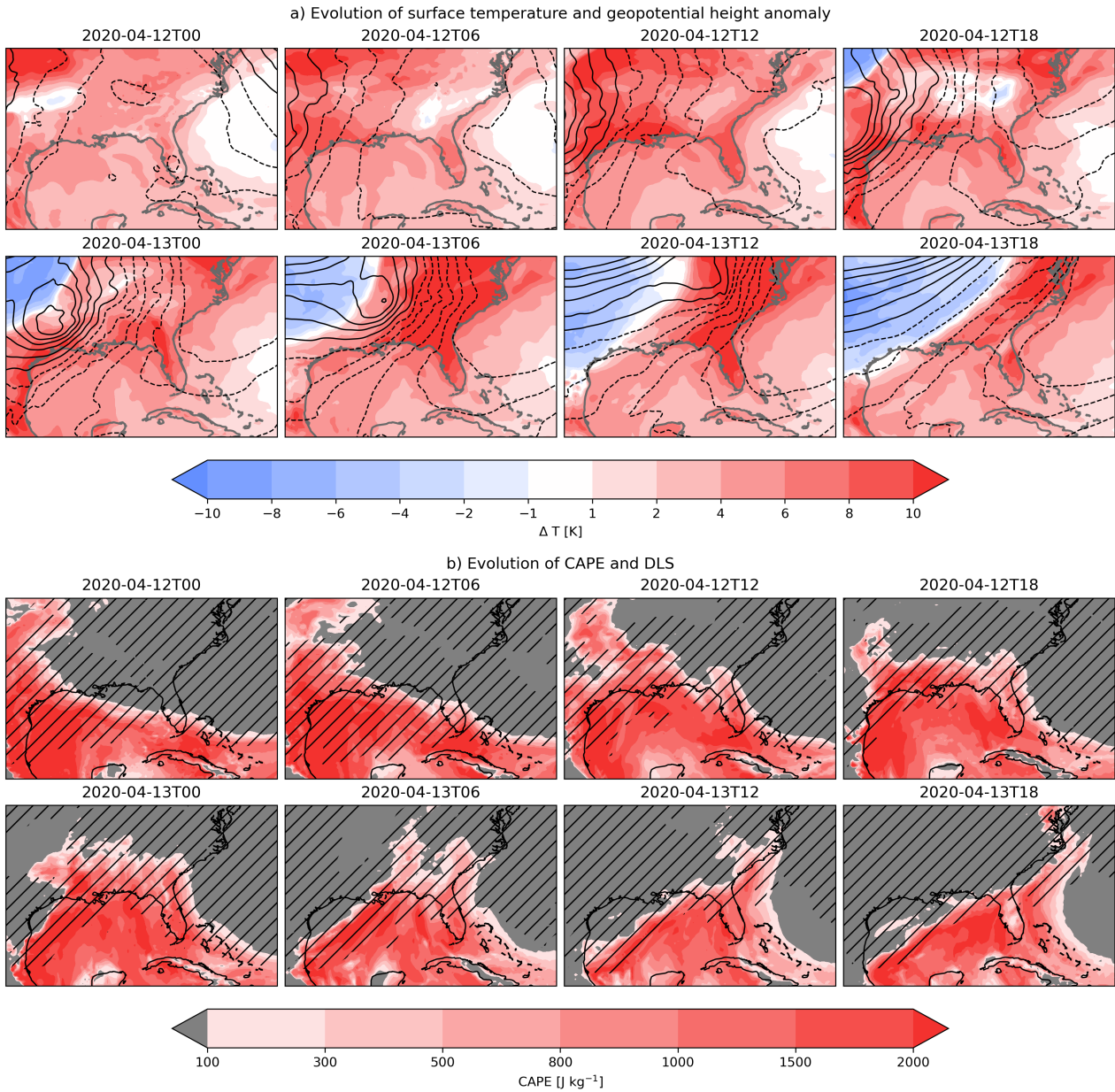


Figure 1: Synoptic situation during the case study on April 12 and 13, showing a deep trough moving across the United States, with anomalously warm temperatures and high CAPE values in the warm sector; a) Climatological geopotential height and surface temperature anomaly, contours indicate positive (dashed) and negative (solid) anomalies of geopotential height in 20 m increments b) CAPE and DLS, hatched area indicates where $DLS > 20\ m\ s^{-1}$.

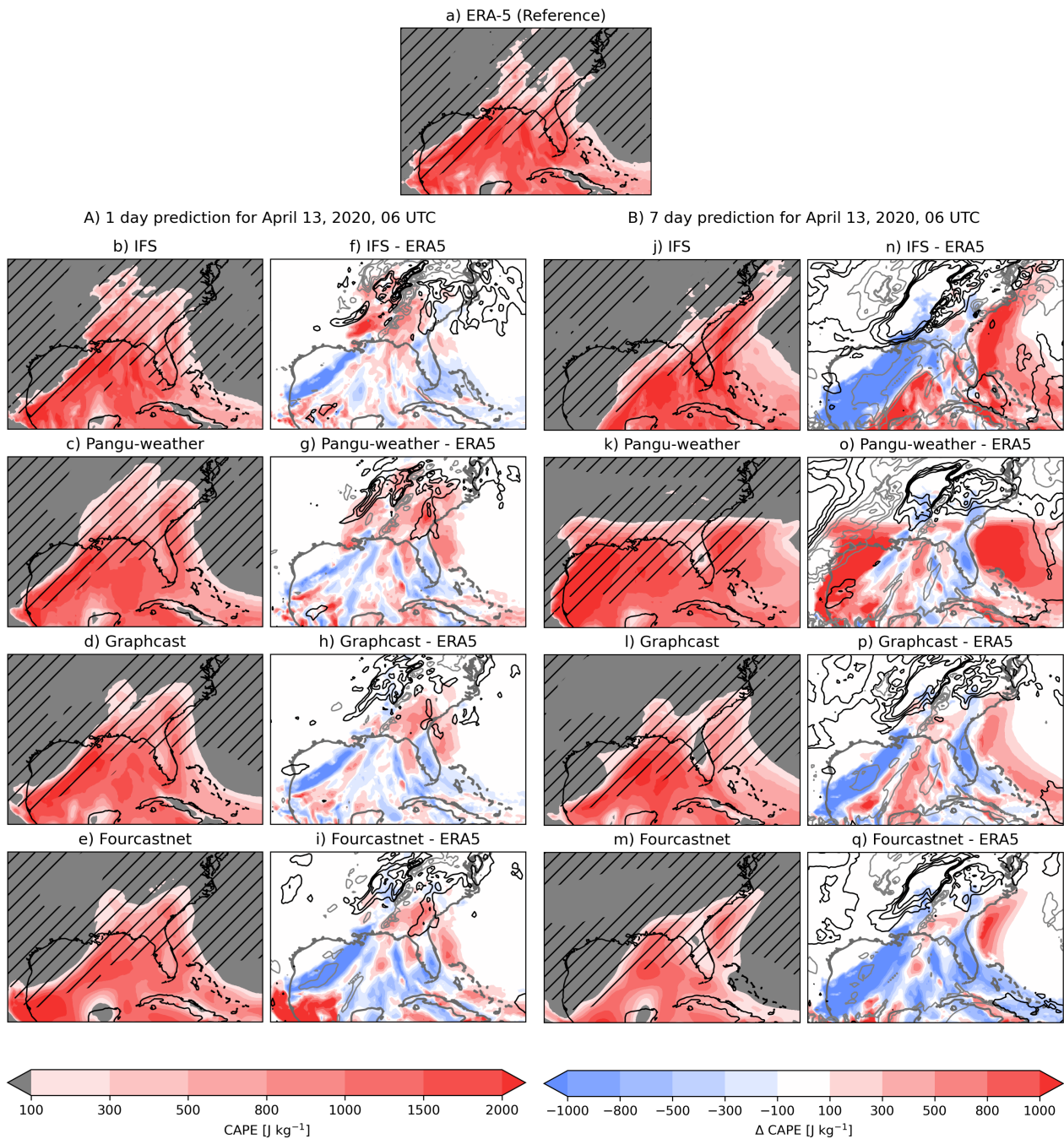


Figure 2: Comparison of forecasts of CAPE and DLS at 1 and 7 days lead-time; a) ERA-5 data of CAPE and DLS on April 13, 2020 at 06 UTC; A) 1 day forecast of CAPE and DLS (b-e) in comparison to ERA5 (f-i) B) 7 day forecast of CAPE and DLS (j-m) in comparison to ERA5 (n-q); hatched area indicates DLS $> 20 \text{ m s}^{-1}$; contours indicated positive (grey) and negative (black) areas of Δ DLS in 5 m s^{-1} increments

mirrored in their marginally increased structure score (see Tables 5 and 6). At this longer lead-time, IFS displaces the event eastwards (Fig. 2j,n), however the magnitude of CAPE values is correct. This leads to large absolute errors (RMSE-IFS 704 J kg⁻¹; for all scores see Table 6). Pangu-Weather’s forecast also suffers from displacement error, while additionally showing a very different spatial structure of the event (Fig. 2k,o, RMSE-Pangu 655 J kg⁻¹). While the coastal areas still have high CAPE values, the slanted shape of the trough is missing and hence the spatial distribution of CAPE is not reproduced well. GraphCast has the best agreement in terms of event structure and location, but overall underestimates the magnitude of CAPE (Fig. 2l,p, RMSE-GraphCast 470 J kg⁻¹). FourCastNet strongly underestimates CAPE and also has the largest degree of smoothing (Fig. 2m,q). It misses most land areas that experience high CAPE and DLS. Nonetheless, we highlight here, that all models capture an area of high CAPE values more than 7 days in advance, in co-location with high DLS.

5 Seasonal and regional analyses

To investigate performance scores, we derive CAPE, DLS and WMS for 5 different regions and their respective convective seasons. Table 4 summarizes the regions’ extent and seasons. We then compute the lead-time-dependent scores for each model.

Region	Latitudes	Longitudes	Months
North America	20/50	250/300	March-September
Europe	35/55	350/30	April-September
Argentina	-40/-25	290/310	September-February
Australia	-35/-20	140/155	September-February

Table 4: Regions

5.1 The North American convective season

Figure 3 depicts the lead-time-dependent scores throughout the entire convective season for the USA. The solid line shows the median score, while the shading shows the interquartile range (IQR). We include here both the models initialized with ERA-5, as well as the operational version, initialized with IFS analysis.

Looking at the RMSE (Fig. 3a) for CAPE, it is noticeable how close the scores of Pangu-Weather, GraphCast, and IFS are. They lie well within each other’s IQR. FourCastNet is a notable exception, performing consistently worse than all other models. GraphCast and Pangu-Weather tend to outperform IFS slightly. Since they are optimized on RMSE (albeit on different variables), we expect them to perform best in this metric. Looking at the BIAS (Fig. 3b), we see a more diverse picture. IFS has a positive BIAS that increases over time. Pangu-Weather has a quite stationary BIAS, centered on 0, but with fluctuations on a 24h-cycle owed to its integration structure using two different models. The original version of GraphCast shows a clear underestimation, which is much improved in the operational version that was re-tuned. FourCastNet shows a strong overestimation, which contrasts with the underestimation in the case study. The seasonal analysis is dominated by the principal convective season in the Great Plains, whereas the case study focuses on a spring convective event in the Southeast. For the FSS₃₀₀ (Fig. 3c), GraphCast and Pangu-Weather are slightly better than IFS at intermediate lead-times. FourCastNet is consistently worse, largely lying outside of the IQR of the other models. In terms of SAL scores, the amplitude score mirrors what we already see in the BIAS

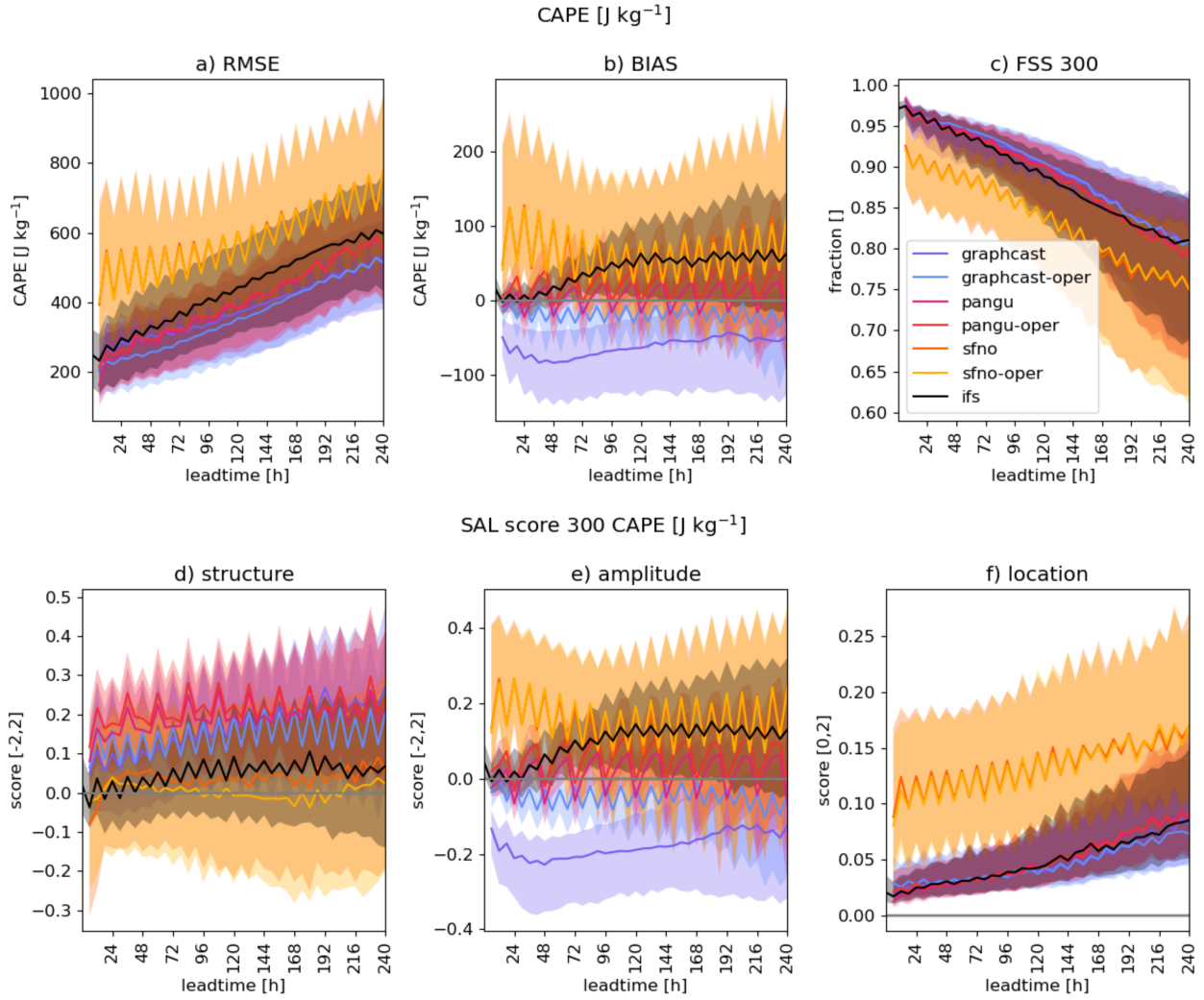


Figure 3: Seasonal evaluation of CAPE for North America shows Pangu-Weather and Graph-Cast performing better than IFS; The top row shows a) RMSE, b) BIAS, c) FSS_{300} ; the bottom row shows the components of the SAL score for $CAPE > 300 \text{ J kg}^{-1}$ d) structure score, e) amplitude score, f) location score; the legend in panel c) indicates which model corresponds to which color; solid line - median, shading - interquartile range

(Fig. 3b,e). The positive structure score shows the smoother behavior of GraphCast and Pangu-Weather (Fig. 3d). It is important to note, that structure, amplitude, and location are not independent of one another. The overall bad performance of FourCastNet impacts the SAL score’s ability to accurately characterize its field. Most notably, the strongly increased location score is evident (Fig. 3f), which may indicate that the overall structures of the CAPE field $>300 \text{ J kg}^{-1}$ are too different to appropriately compare to ERA5. The other models behave very similarly regarding the location score and perform much better than FourCastNet. The location score shows the largest dependence on lead-time, steadily increasing (Fig. 3f). Overall IFS has scores close to ‘0’ in both structure and amplitude, while the location score shows the strongest deterioration over lead-time. The smoother fields of the neural weather models are indicated with positive values in the structure score, indicating too large areas with too high values. They match IFS’s performance in terms of location.

A clear pattern visible in all models is a regular spikiness. For Pangu-Weather this is in a 24-hour frequency, indicating the impact of the change between the 6h- and 24h-integration models. Given that the initializations of all models are twice a day, regular variation in e.g., BIAS can be attributed to the strong diurnal cycle of CAPE, which depends on the diurnal cycle of temperature (Leon, 2018; Lawson and Gallus Jr, 2016). By separating the data into the 00 UTC and 12 UTC initializations, we can clearly identify the diurnal cycle (figure not shown). The models tend to perform better at night and in the early morning when CAPE is naturally low. The errors are higher during the day and in the evening when peak CAPE values occur. For Pangu-Weather, both the diurnal cycle of CAPE, as well as the switch between its two integration models every 24 hours impact the scores.

Given the similarity between the initializations with ERA5 and the initializations with IFS analysis for Pangu-Weather and FourCastNet, we focus the next analyses on the initializations with IFS. This mimics how the models are run in an operational context. Since GraphCast (initialized with ERA-5) and GraphCast-operational (initialized with IFS) are two different model versions, we maintain both.

5.2 The impact of thermodynamic conversions

It is noticeable, how FourCastNet behaves differently from Pangu-Weather and GraphCast. One of the core differences in between the models is how they predict moisture. Q is used most commonly, but due to the relatively strong boundedness, RH has been shown to generalize better in some machine learning applications (Beucler et al., 2024a; Lin et al., 2024). This is most applicable for large domain shifts in a changing climate, where Q is no longer well-constrained. At the weather timescale, Q can be assumed to be in a stable value range. FourCastNet predicts RH; to calculate CAPE RH needs to be converted to Q. The conversion is dependent on the temperature and pressure, making this an additional processing step, where forecast errors can compound. To quantify this effect, we additionally compare all models’ RMSE and BIAS for RH, Q and T. Figure 4 shows this for the US convective season.

The RMSE (Fig. 4a) and BIAS (Fig. 4b) of temperature are quite similar across all models, indicating that the large differences in CAPE are not primarily owed to the temperature field. At short lead-times FourCastNet does perform worse, but only by a small margin. Looking at Q, it becomes evident that FourCastNet not only has a larger RMSE (Fig. 4c) but also consistently overestimates Q (Fig. 4d), which does not improve much at short lead-times. Considering that Q has to be converted from RH in FourCastNet, we additionally investigate RH for all models. It becomes evident, that despite this being the natively predicted variable, FourCastNet also

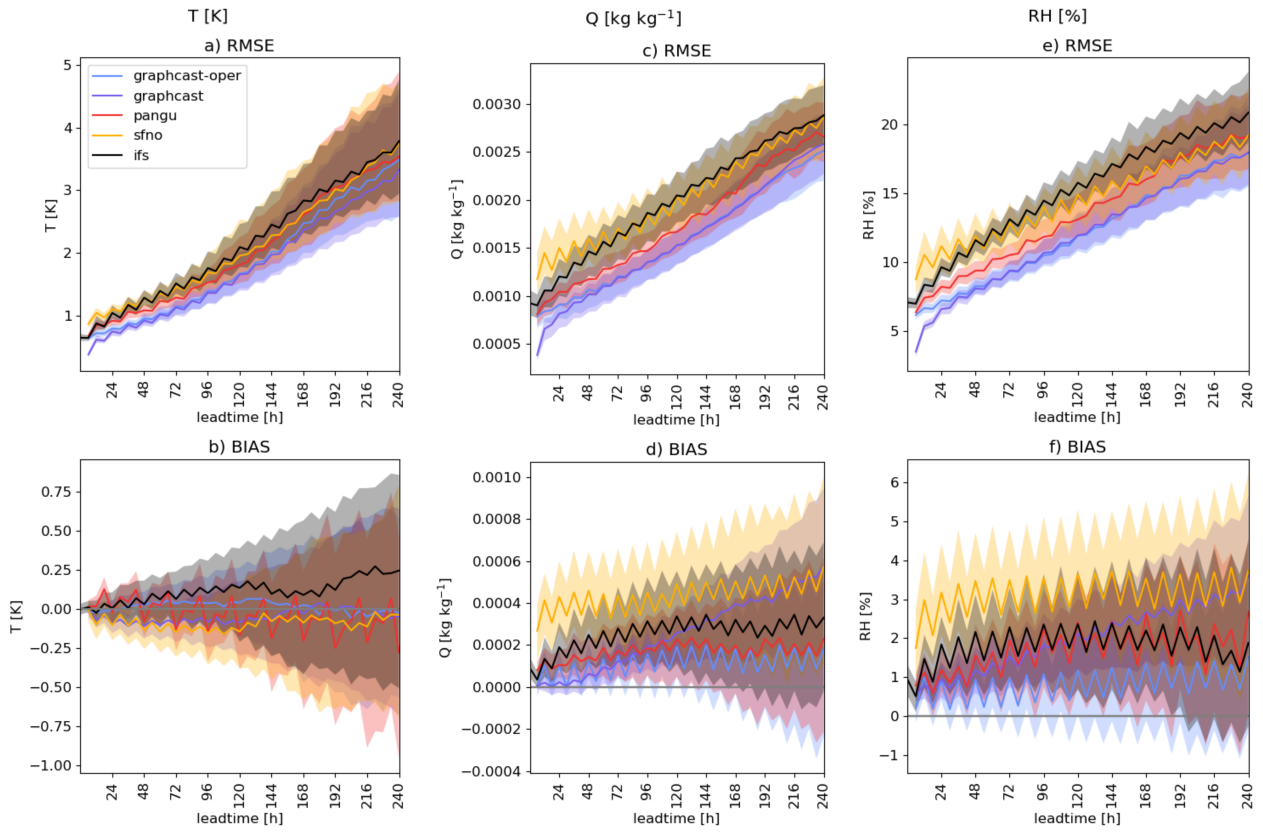


Figure 4: Seasonal evaluation of temperature, specific and relative humidity for North America shows strong biases and larger RMSE in moisture for FourCastNet; a,b) Temperature, c,d) specific and e,f) relative humidity scores at 925 hPa

does not perform particularly well for RH, the BIAS (Fig. 4f) remains consistently positive. GraphCast-oper and Pangu-Weather consistently have a lower RMSE and BIAS (Fig. 4e,f), although this is a converted variable for their models. Consequently, FourCastNet suffers from a double penalty - the moderately good RH undergoes further conversion to Q before being integrated into the computation of CAPE. The moisture is a key component in determining the lifting condensation level, which strongly impacts the integral of CAPE. The compounding errors here greatly affect the final computation of CAPE.

5.3 Global convective hotspots

We next compare the models' performance in a number of additional convectively active regions. In addition to the USA, we investigate Europe, Argentina, and Australia. Figure 5 depicts the RMSE, BIAS, and FSS₃₀₀ for CAPE, while Fig. 6 shows the same for WMS.

In a first approximation, we can see that the RMSE is highest in North America (Fig. 5a). This is partially driven by the overall magnitude of CAPE values during the 2020 convective seasons. The magnitude of CAPE impacts the FSS₃₀₀, as the FSS generally decreases, as the threshold approaches the tail end of the overall value distribution (see also the systematic difference between FSS₃₀₀ and FSS₁₀₀₀ in Fig. 5). Hence it is consistent that the FSS₃₀₀ is overall best in North America (Fig. 5c), where 300 J kg⁻¹ corresponds to the 63 percentile of the distribution, while a CAPE value 300 of J kg⁻¹ is between the 82 and 86 percentile for all other regions.

FourCastNet generally performs worse and has a wider range of performance scores than the other models. This is primarily driven by the quality of its RH forecast. Australia is an outlier here, where FourCastNet is able to achieve similar RMSE (Fig. 5m) to the other models, albeit with a very large IQR. The lower RMSE is mirrored in RH, which is predicted better in this region (figure not shown).

In all regions, GraphCast-oper shows the lowest RMSE (Fig. 5a,e,i,m) and over most lead-times the highest FSS₃₀₀ (Fig. 5c,g,k,o), with Pangu-Weather falling in between GraphCast-oper and IFS. GraphCast has a greater bias than GraphCast-oper, but largely achieves similarly skillful scores. Despite the small differences, the high consistency across multiple regions shows this as systematic behavior.

To finally investigate the capability of AI-models to produce convective environments compounding CAPE and DLS, we also look at the scores of WMS in Fig. 6. The overall performance is strongly driven by CAPE, which is more challenging to forecast than DLS. Overall, GraphCast-oper achieves the lowest RMSE (Fig. 6a,e,i,m) and highest FSS₃₀₀ (Fig. 6c,g,k,o), closely followed by Pangu-Weather. IFS performs very similarly to GraphCast-oper and Pangu-Weather in terms of FSS₃₀₀, but falls further behind in the RMSE. GraphCast specifically performs worse on the FSS₅₀₀ (Fig. 6d,h,l,p), indicating difficulties in capturing the tail of the distribution. FourCastNet generally performs worse, with a very large IQR. Most striking are the strong BIAS in Europe and the consistently high RMSE at short lead-times. FourCastNet appears unable to improve its forecasts at short lead-times to the degree that the other models do.

6 Discussion and Conclusion

As shown in Section 5, Pangu-Weather, GraphCast-oper, and GraphCast are capable of producing realistic forecasts of the mesoscale convective environment at medium-range lead-times in a matter of minutes and perform similarly to IFS. The original version of GraphCast has a larger bias for CAPE and decreased FSS, which is greatly improved in the operationally tuned

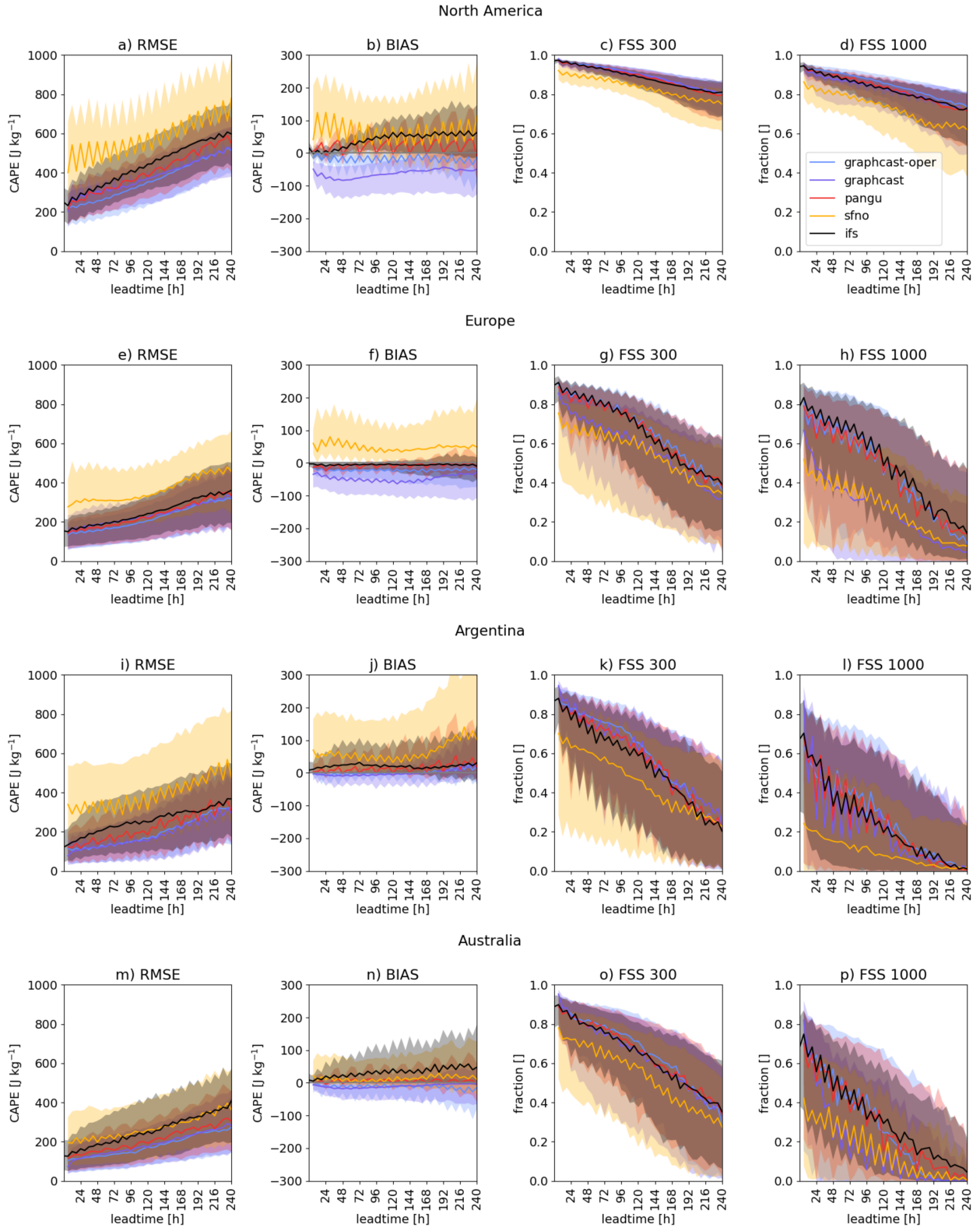


Figure 5: Seasonal evaluation of CAPE in North America (a-d), Europe (e-h), Argentina (i-l) and Australia (m-p) shows good performance of GraphCast and Pangu-Weather; solid line depicts median of score, the IQR is shown in shading

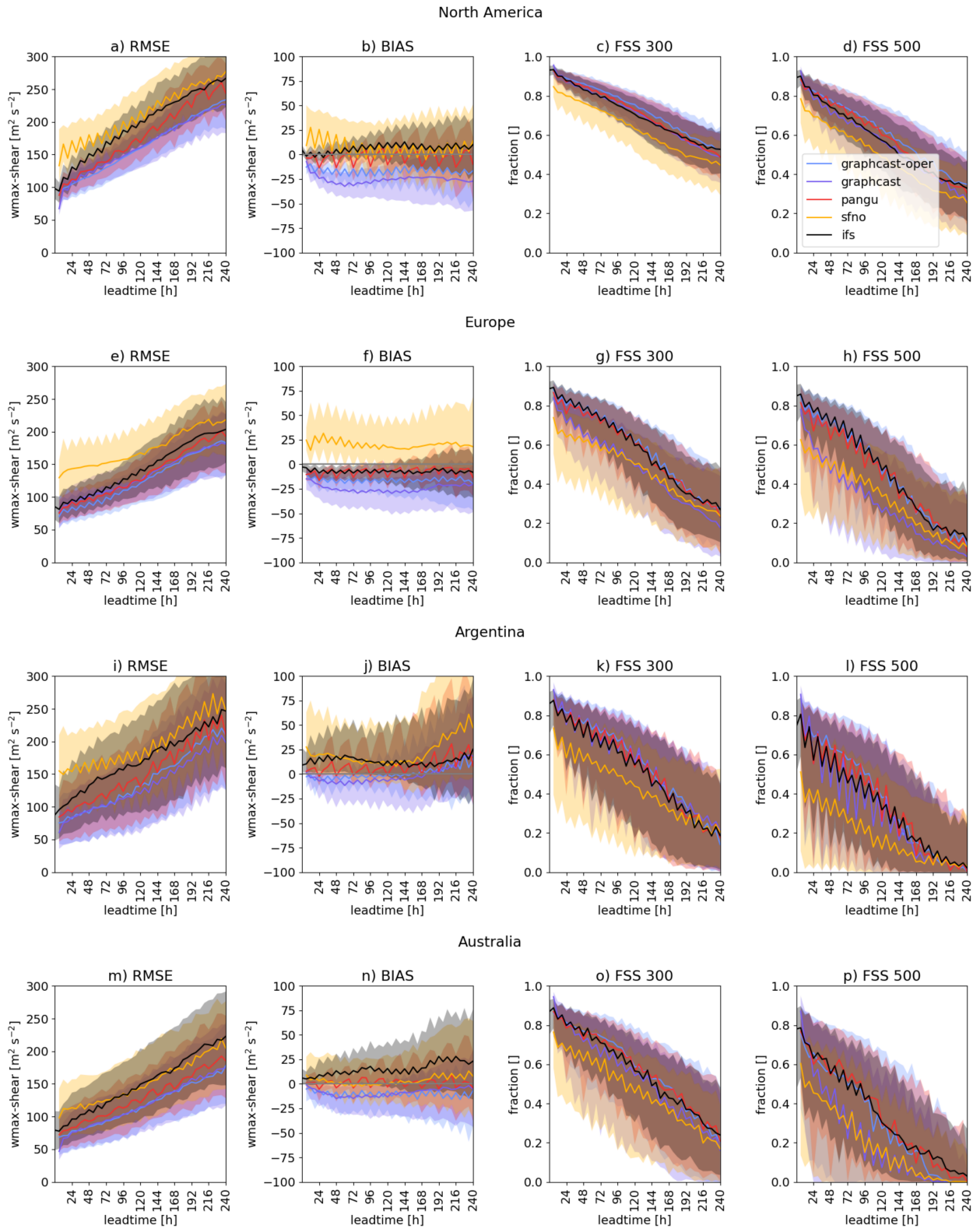


Figure 6: Seasonal evaluation of WMS in North America (a-d), Europe (e-h), Argentina (i-l) and Australia (m-p) shows good performance of GraphCast and Pangu-Weather; solid line depicts median of score, the IQR is shown in shading

version. Since the fine-tuning period includes 2020, a realistic ongoing performance can be expected in between these two score ranges (personal communication with Matthew Chantry). Pangu-Weather shows only minor differences between the initializations from ERA-5 and IFS analysis. FourCastNet has the strongest deficiencies, partially owed to the additional processing step from RH to Q. However, as Section 5.2 shows, forecasting errors in convective parameters are also owed to issues in forecasting moisture overall. With GraphCast and Pangu-Weather providing reasonable RH values derived from Q, we conclude that RH is not necessarily a worse choice than Q, but rather that “FourCastNet v2 small” specifically has issues in forecasting moisture. The best choice in moisture variable depends on the application, as every thermodynamic conversion in a non-physical model comes with additional uncertainty.

The evaluation of different regions shows the global capability of Pangu-Weather and GraphCast in particular. In spite of regional performance differences, the ranking of models remains stable, with GraphCast-oper consistently performing best in terms of RMSE, followed by Pangu-Weather and IFS. These models score very similarly, and their systematic differences are smaller than the uncertainty of the initialization. For the FSS, Pangu-Weather and GraphCast-oper are able to achieve similar scores to IFS, but do not consistently outperform it. This highlights how the RMSE that the models are trained to minimize is an incomplete perspective on model performance.

Another notable point is the perceived discrepancy between the case study and the evaluation of the North American convective season. The case study takes place in spring and focuses on the Southeast of the US, while the bulk of the convective season is driven by the Great Plains in summer. A single case never allows for a comprehensive conclusion on model performance. Particularly the moderately good performance of FourCastNet in this instance is not typical when over most of the summer season, RH and subsequently CAPE are largely overestimated. An additional example case during the summer is provided in the supplemental material (see Fig. 7). The shortcomings of Pangu-Weather in forecasting the event structure at longer lead-times are also limited to this singular case study. As the seasonal evaluation shows, Pangu-Weather does not systematically perform worse than IFS at 7 days lead-time. This highlights the necessity to evaluate a larger sample of cases, before drawing conclusions on the performance of neural weather models. While a single convective season is still rather short, the consistency of the results across four different global regions indicates robustness in our evaluation.

Despite the shortcomings of deriving CAPE from vertically coarse pressure levels, the promising results of GraphCast and Pangu-Weather indicate that CAPE is a worthwhile prediction variable. Predicting CAPE directly instead of deriving it from coarse pressure levels, would likely be the most skillful approach. Foundational models in particular, such as Aurora or ClimaX, are designed for easier addition of variables after the main training of the model. While forecasting convective environments is a large step closer to application-oriented forecasting, it still lacks the specificity of impact-oriented hazard predictions, such as directly predicting the likelihood of tornado, hail, gust, lightning or flashflood occurrence. Rapid progress in down-scaling through super-resolution may enable direct hazard forecasts in the foreseeable future. At the current state, the vertical coarseness limits the number of convectively relevant variables that can be derived. We refrained from evaluating near-surface shear or helicity due to the limited resolution. However, these are key metrics for the assessment of convective hazards, especially tornadoes. With forecasters exploiting a whole myriad of convective parameters, it remains to be seen how practicable the direct prediction of convective parameters is. Taking this first step of deriving CAPE and DLS in neural weather models already provides

useful information for severe convective outlooks, which are key for severe weather warnings. This highlights how application-oriented products can be derived from AI-generated forecasts, with similar skill to operational numerical models. Especially with their very short runtime, they are able to deliver very timely forecasts at a low computational cost. This step towards process-based assessment of neural weather models is crucial for the future development of hazard-driven applications.

Acknowledgements

We thank Zied Ben Bouallegue and Matthew Chantry for the insightful discussions on the current state of neural weather forecasting and the particular challenges of operational forecasting. We also thank Louis Poulain-Auzéau for his work on installing the neural weather models. Olivia Martius acknowledges support from the Swiss National Science Foundation project No. CRSII5_201792.

Author contributions

Monika Feldmann processed the data to derive convective parameters and evaluate their performance, create the visualizations and wrote the main body of the manuscript. Tom Beucler provided the computational resources necessary for the project, expertise on the properties of neural weather models and their evaluation and reviewed the manuscript. Milton Gomez produced the FourCastNet predictions, assisted with computational aspects of the project, provided valuable expertise and reviewed the manuscript. Olivia Martius co-designed the project, supervised the project and reviewed the manuscript.

Statement of data and code availability

The IFS, ERA-5, Pangu-Weather and GraphCast data were accessed through “Weatherbench2” (Rasp et al., 2024). FourCastNet predictions were computed with the code release of ECMWF (ECMWF, 2023). The code used to process the forecast data and produce the visualizations can be accessed at <https://github.com/feldmann-m/AI-storm>.

Competing interests

Monika Feldmann and Olivia Martius are in positions funded by the Mobiliar Insurance Group. This funding source played no role in any part of the study.

References

- M. Barratt. The new ECMWF interpolation package MIR. *ECMWF*, Aug. 2017. doi: 10.21957/h20rz8. URL <https://www.ecmwf.int/en/newsletter/152/computing/new-ecmwf-interpolation-package-mir>.
- F. Battaglioli, P. Groenemeijer, I. Tsonevsky, and T. Púčik. Forecasting large hail and lightning using additive logistic regression models and the ecmwf reforecasts. *Natural Hazards and Earth System Sciences*, 23(12):3651–3669, 2023. doi: 10.5194/nhess-23-3651-2023. URL <https://nhess.copernicus.org/articles/23/3651/2023/>.

- B. Beddoes. Ranking the easter 2020 tornado outbreak versus the worst outbreaks in history; accessed on 2024-05-28, 2020. URL <https://www.whsv.com/content/news/Ranking-the-Easter-2020-outbreak-versus-the-worst-outbreaks-in-history-569861941.html>.
- T. Beucler, P. Gentine, J. Yuval, A. Gupta, L. Peng, J. Lin, S. Yu, S. Rasp, F. Ahmed, P. O’Gorman, J. D. Neelin, N. J. Lutsko, and M. Pritchard. Climate-invariant machine learning. *Science Advances*, 10(6), Feb. 2024a. doi: 10.1126/sciadv.adj7250. URL <https://www.science.org/doi/full/10.1126/sciadv.adj7250>.
- T. Beucler, E. Koch, S. Kotlarski, D. Leutwyler, A. Michel, and J. Koh. Next-generation earth system models: Towards reliable hybrid models for weather and climate applications, 2024b.
- L. Bevere and A. Weigel. Sigma: Natural catastrophes in 2020: secondary perils in the spotlight, but don’t forget primary-peril risks. *Swiss Re Institute*, 1, 2021. URL <https://www.swissre.com/dam/jcr:706844c8-31c1-44ad-8e32-0166c93d9466/sigma-1-2021-en.pdf>.
- K. Bi, L. Xie, H. Zhang, X. Chen, X. Gu, and Q. Tian. Accurate medium-range global weather forecasting with 3D neural networks. *Nature*, 619(7970):533–538, July 2023. ISSN 1476-4687. doi: 10.1038/s41586-023-06185-3. URL <https://www.nature.com/articles/s41586-023-06185-3>. Publisher: Nature Publishing Group.
- C. Bodnar, W. P. Bruinsma, A. Lucic, M. Stanley, J. Brandstetter, P. Garvan, M. Riechert, J. Weyn, H. Dong, A. Vaughan, J. K. Gupta, K. Tambiratnam, A. Archibald, E. Heider, M. Welling, R. E. Turner, and P. Perdikaris. Aurora: A foundation model of the atmosphere, 2024.
- M. Bonavita. On some limitations of data-driven weather forecasting models, 2023.
- B. Bonev, T. Kurth, C. Hundt, J. Pathak, M. Baust, K. Kashinath, and A. Anandkumar. Spherical Fourier neural operators: Learning stable dynamics on the sphere. In A. Krause, E. Brunskill, K. Cho, B. Engelhardt, S. Sabato, and J. Scarlett, editors, *Proceedings of the 40th International Conference on Machine Learning*, volume 202 of *Proceedings of Machine Learning Research*, pages 2806–2823. PMLR, 23–29 Jul 2023. URL <https://proceedings.mlr.press/v202/bonev23a.html>.
- Z. B. Bouallègue, M. C. A. Clare, L. Magnusson, E. Gascón, M. Maier-Gerber, M. Janoušek, M. Rodwell, F. Pinault, J. S. Dramsch, S. T. K. Lang, B. Raoult, F. Rabier, M. Chevalier, I. Sandu, P. Dueben, M. Chantry, and F. Pappenberger. The rise of data-driven weather forecasting: A first statistical assessment of machine learning-based weather forecasts in an operational-like context. *Bulletin of the American Meteorological Society*, 2024. doi: 10.1175/BAMS-D-23-0162.1. URL <https://journals.ametsoc.org/view/journals/bams/aop/BAMS-D-23-0162.1/BAMS-D-23-0162.1.xml>.
- P. Bougeault, Z. Toth, C. Bishop, B. Brown, D. Burridge, D. H. Chen, B. Ebert, M. Fuentes, T. M. Hamill, K. Mylne, J. Nicolau, T. Paccagnella, Y.-Y. Park, D. Parsons, B. Raoult, D. Schuster, P. S. Dias, R. Swinbank, Y. Takeuchi, W. Tennant, L. Wilson, and S. Worley. The thorpex interactive grand global ensemble. *Bulletin of the American Meteorological Society*, 91(8):1059 – 1072, 2010. doi: 10.1175/2010BAMS2853.1. URL https://journals.ametsoc.org/view/journals/bams/91/8/2010bams2853_1.xml.
- S. Bowen, B. Kerschner, and J. Zheng Ng. Natural catastrophe and climate report 2023. *Gallagher Re*, 2024. URL <https://www.ajg.com/gallagherre/-/media/files/gallagher/>

[gallagherre/news-and-insights/2024/january/natural_catastrophe_and_climate_report_2023.pdf](#).

- H. Brooks, P. Marsh, A. Kowaleski, P. Groenemeijer, T. Thompson, C. Schwartz, C. Shafer, A. Kolodziej, N. Dahl, and D. Buckley. Evaluation of european storm forecast experiment (estofex) forecasts. *Atmospheric Research*, 100(4):538–546, 2011. ISSN 0169-8095. doi: <https://doi.org/10.1016/j.atmosres.2010.09.004>. URL <https://www.sciencedirect.com/science/article/pii/S0169809510002425>. 5th European Conference on Severe Storms.
- H. E. Brooks. Severe thunderstorms and climate change. *Atmospheric Research*, 123:129–138, 2013. ISSN 0169-8095. doi: 10.1016/j.atmosres.2012.04.002. URL [10.1016/j.atmosres.2012.04.002](https://doi.org/10.1016/j.atmosres.2012.04.002). Publisher: Elsevier B.V.
- H. E. Brooks, J. W. Lee, and J. P. Craven. The spatial distribution of severe thunderstorm and tornado environments from global reanalysis data. *Atmospheric Research*, 67-68:73–94, 2003. ISSN 01698095. doi: 10.1016/S0169-8095(03)00045-0. ISBN: 0169-8095.
- G. Brunet, D. B. Parsons, D. Ivanov, B. Lee, P. Bauer, N. B. Bernier, V. Bouchet, A. Brown, A. Busalacchi, G. C. Flatter, R. Goffier, P. Davies, B. Ebert, K. Gutbrod, S. Hong, P. K. Kenabatho, H.-J. Koppert, D. Lesolle, A. H. Lynch, J.-F. Mahfouf, L. Ogallo, T. Palmer, K. Petty, D. Schulze, T. G. Shepherd, T. F. Stocker, A. Thorpe, and R. Yu. Advancing weather and climate forecasting for our changing world. *Bulletin of the American Meteorological Society*, 104(4):E909 – E927, 2023. doi: 10.1175/BAMS-D-21-0262.1. URL <https://journals.ametsoc.org/view/journals/bams/104/4/BAMS-D-21-0262.1.xml>.
- A. J. Charlton-Perez, H. F. Dacre, S. Driscoll, S. L. Gray, B. Harvey, N. J. Harvey, K. M. R. Hunt, R. W. Lee, R. Swaminathan, R. Vandaale, and A. Volonté. Do AI models produce better weather forecasts than physics-based models? A quantitative evaluation case study of Storm Ciarán. *npj Climate and Atmospheric Science*, 7, 2024. doi: 10.1038/s41612-024-00638-w.
- L. Chen, X. Zhong, F. Zhang, Y. Cheng, Y. Xu, Y. Qi, and H. Li. FuXi: a cascade machine learning forecasting system for 15-day global weather forecast. *npj Climate and Atmospheric Science*, 6(1):1–11, Nov. 2023. ISSN 2397-3722. doi: 10.1038/s41612-023-00512-1. URL <https://www.nature.com/articles/s41612-023-00512-1>. Publisher: Nature Publishing Group.
- Copernicus Services. Surface air temperature for march 2020, accessed on 2024-05-24, 2020. URL <https://climate.copernicus.eu/surface-air-temperature-march-2020>.
- A. Dean and G. Dial. Day 4-8 severe weather outlook issued on apr 8, 2020; accessed on 2024-05-24, 2020. URL https://www.spc.noaa.gov/products/exper/day4-8/archive/2020/day4-8_20200408.html.
- I. Ebert-Uphoff and K. Hilburn. The outlook for ai weather prediction. *Nature Briefing*, 2023. doi: 10.1038/d41586-023-02084-9.
- ECMWF. ai-models; last accessed: 12-12-2023, 2023. URL <https://github.com/ecmwf-lab/ai-models>.
- E. Gilleland. Testing competing precipitation forecasts accurately and efficiently: The spatial prediction comparison test. *Monthly Weather Review*, 141(1):340 – 355, 2013. doi: 10.1175/MWR-D-12-00155.1. URL <https://journals.ametsoc.org/view/journals/mwre/141/1/mwr-d-12-00155.1.xml>.

- E. Gilleland, D. Ahijevych, B. G. Brown, B. Casati, and E. E. Ebert. Intercomparison of spatial forecast verification methods. *Weather and Forecasting*, 24(5):1416 – 1430, 2009. doi: 10.1175/2009WAF2222269.1. URL https://journals.ametsoc.org/view/journals/wefo/24/5/2009waf2222269_1.xml.
- M. Govett, B. Bah, P. Bauer, D. Berod, V. Bouchet, S. Corti, C. Davis, Y. Duan, T. Graham, Y. Honda, A. Hines, M. Jean, J. Ishida, B. Lawrence, J. Li, J. Luterbacher, C. Muroi, K. Rowe, M. Schultz, M. Visbeck, and K. Williams. Exascale computing and data handling: Challenges and opportunities for weather and climate prediction. *Bulletin of the American Meteorological Society*, 2024. doi: 10.1175/BAMS-D-23-0220.1. URL <https://journals.ametsoc.org/view/journals/bams/aop/BAMS-D-23-0220.1/BAMS-D-23-0220.1.xml>.
- T. Haiden, M. Janousek, F. Vitart, L. Ferranti, and F. Prates. Evaluation of ecmwf forecasts, including the 2019 upgrade, 11/2019 2019. URL <https://www.ecmwf.int/node/19277>.
- G. J. Hakim and S. Masanam. Dynamical tests of a deep-learning weather prediction model. *Artificial Intelligence for the Earth Systems*, 2024. doi: 10.1175/AIES-D-23-0090.1. URL <https://journals.ametsoc.org/view/journals/aies/aop/AIES-D-23-0090.1/AIES-D-23-0090.1.xml>.
- H. Hersbach, B. Bell, P. Berrisford, S. Hirahara, A. Horányi, J. Muñoz-Sabater, J. Nicolas, C. Peubey, R. Radu, D. Schepers, A. Simmons, C. Soci, S. Abdalla, X. Abellan, G. Balsamo, P. Bechtold, G. Biavati, J. Bidlot, M. Bonavita, G. De Chiara, P. Dahlgren, D. Dee, M. Diamantakis, R. Dragani, J. Flemming, R. Forbes, M. Fuentes, A. Geer, L. Haimberger, S. Healy, R. J. Hogan, E. Hólm, M. Janisková, S. Keeley, P. Laloyaux, P. Lopez, C. Lupu, G. Radnoti, P. de Rosnay, I. Rozum, F. Vamborg, S. Villaume, and J.-N. Thépaut. The era5 global reanalysis. *Quarterly Journal of the Royal Meteorological Society*, 146(730):1999–2049, 2020. doi: <https://doi.org/10.1002/qj.3803>. URL <https://rmets.onlinelibrary.wiley.com/doi/abs/10.1002/qj.3803>.
- R. A. Houze. Chapter 8 - cumulonimbus and severe storms. In R. A. Houze, editor, *Cloud Dynamics*, volume 104 of *International Geophysics*, pages 187–236. Academic Press, 2014. doi: <https://doi.org/10.1016/B978-0-12-374266-7.00008-1>. URL <https://www.sciencedirect.com/science/article/pii/B9780123742667000081>.
- J. Jeppesen. European met services pool resources to intensify use of AI in weather prediction, Jan. 2024. URL <https://www.ecmwf.int/en/about/media-centre/news/2024/european-met-services-pool-resources-intensify-use-ai-weather>.
- M. Kunz. The skill of convective parameters and indices to predict isolated and severe thunderstorms. *Natural Hazards and Earth System Sciences*, 7(2):327–342, 2007. doi: 10.5194/nhess-7-327-2007. URL <https://nhess.copernicus.org/articles/7/327/2007/>.
- W. Ladwig. wrf-python (version 1.3.4.1) [software], 2017. URL <https://doi.org/10.5065/D6W094P1>.
- R. Lam, A. Sanchez-Gonzalez, M. Willson, P. Wirnsberger, M. Fortunato, F. Alet, S. Ravuri, T. Ewalds, Z. Eaton-Rosen, W. Hu, A. Merose, S. Hoyer, G. Holland, O. Vinyals, J. Stott, A. Pritzel, S. Mohamed, and P. Battaglia. Learning skillful medium-range global weather forecasting. *Science*, 382(6677):1416–1421, Dec. 2023. doi: 10.1126/science.adi2336. URL <https://www.science.org/doi/full/10.1126/science.adi2336>. Publisher: American Association for the Advancement of Science.

- S. Lang, M. Alexe, M. Chantry, J. Dramsch, F. Pinault, B. Raoult, M. C. A. Clare, C. Lessig, M. Maier-Gerber, L. Magnusson, Z. B. Bouallègue, A. P. Nemesio, P. D. Dueben, A. Brown, F. Pappenberger, and F. Rabier. Aifs - ecmwf’s data-driven forecasting system, 2024.
- J. R. Lawson and W. A. Gallus Jr. Adapting the sal method to evaluate reflectivity forecasts of summer precipitation in the central united states. *Atmospheric Science Letters*, 17(10): 524–530, 2016. doi: <https://doi.org/10.1002/asl.687>. URL <https://rmets.onlinelibrary.wiley.com/doi/abs/10.1002/asl.687>.
- J. A. P. Leon. Addressing biases in near-surface forecasts, Oct. 2018. URL <https://www.ecmwf.int/en/newsletter/157/meteorology/addressing-biases-near-surface-forecasts>.
- J. Lin, M. A. Bhourri, T. Beucler, S. Yu, and M. Pritchard. Stress-testing the coupled behavior of hybrid physics-machine learning climate simulations on an unseen, warmer climate, 2024.
- P. Markowski and Y. Richardson. *Mesoscale Meteorology in Midlatitudes*. Wiley-Blackwell, 2010. ISBN 978-0-470-74213-6. doi: 10.1002/9780470682104.
- C. A. Mensch. *Impacts of Vertical Grid Resolution on the Representation of a Convective Environment*. PhD thesis, University of North Dakota, 2021 2021. URL <https://www.proquest.com/dissertations-theses/impacts-vertical-grid-resolution-on/docview/2549273827/se-2>. Copyright - Database copyright ProQuest LLC; ProQuest does not claim copyright in the individual underlying works; Zuletzt aktualisiert - 2023-03-08.
- M. P. Mittermaier. A “meta” analysis of the fractions skill score: The limiting case and implications for aggregation. *Monthly Weather Review*, 149(10):3491 – 3504, 2021. doi: 10.1175/MWR-D-18-0106.1. URL <https://journals.ametsoc.org/view/journals/mwre/149/10/MWR-D-18-0106.1.xml>.
- T. Nguyen, J. Brandstetter, A. Kapoor, J. K. Gupta, and A. Grover. ClimaX: A foundation model for weather and climate, July 2023. URL <http://arxiv.org/abs/2301.10343>. arXiv:2301.10343 [cs].
- L. Olivetti and G. Messori. Advances and prospects of deep learning for medium-range extreme weather forecasting. *Geoscientific Model Development*, 17(6):2347–2358, 2024a. doi: 10.5194/gmd-17-2347-2024. URL <https://gmd.copernicus.org/articles/17/2347/2024/>.
- L. Olivetti and G. Messori. Do data-driven models beat numerical models in forecasting weather extremes? a comparison of ifs hres, pangu-weather and graphcast. *EGUsphere*, 2024:1–35, 2024b. doi: 10.5194/egusphere-2024-1042. URL <https://egusphere.copernicus.org/preprints/2024/egusphere-2024-1042/>.
- S. Rasp, S. Hoyer, A. Merose, I. Langmore, P. Battaglia, T. Russel, A. Sanchez-Gonzalez, V. Yang, R. Carver, S. Agrawal, M. Chantry, Z. B. Bouallegue, P. Dueben, C. Bromberg, J. Sisk, L. Barrington, A. Bell, and F. Sha. Weatherbench 2: A benchmark for the next generation of data-driven global weather models, 2024.
- Storm Prediction Center. 20200412’s storm reports (20200412 1200 utc - 20200413 1159 utc); accessed on 2024-05-28, 2020a. URL <https://www.spc.noaa.gov/exper/archive/event.php?date=20200412>.
- Storm Prediction Center. 20200413’s storm reports (20200413 1200 utc - 20200414 1159 utc); accessed on 2024-05-28, 2020b. URL <https://www.spc.noaa.gov/exper/archive/event.php?date=20200413>.

- M. Taszarek, H. E. Brooks, and B. Czernecki. Sounding-Derived Parameters Associated with Convective Hazards in Europe. *Monthly Weather Review*, 145(4):1511–1528, Apr. 2017. ISSN 1520-0493, 0027-0644. doi: 10.1175/MWR-D-16-0384.1. URL <https://journals.ametsoc.org/view/journals/mwre/145/4/mwr-d-16-0384.1.xml>. Publisher: American Meteorological Society Section: Monthly Weather Review.
- M. Taszarek, J. T. Allen, P. Groenemeijer, R. Edwards, H. E. Brooks, V. Chmielewski, and S.-E. Enno. Severe Convective Storms across Europe and the United States. Part I: Climatology of Lightning, Large Hail, Severe Wind, and Tornadoes. *Journal of Climate*, 33(23):10239–10261, Dec. 2020. ISSN 0894-8755, 1520-0442. doi: 10.1175/JCLI-D-20-0345.1. URL <https://journals.ametsoc.org/view/journals/clim/33/23/jcliD200345.xml>. Publisher: American Meteorological Society Section: Journal of Climate.
- M. Taszarek, J. T. Allen, M. Marchio, and H. E. Brooks. Global climatology and trends in convective environments from ERA5 and rawinsonde data. *npj Climate and Atmospheric Science*, 4(1):1–11, June 2021. ISSN 2397-3722. doi: 10.1038/s41612-021-00190-x. URL <https://www.nature.com/articles/s41612-021-00190-x>. Number: 1 Publisher: Nature Publishing Group.
- J.-N. Thepaut and P. Courtier. Four-dimensional variational data assimilation using the adjoint of a multilevel primitive-equation model. *Quarterly Journal of the Royal Meteorological Society*, 117(502):1225–1254, 1991. doi: <https://doi.org/10.1002/qj.49711750206>. URL <https://rmets.onlinelibrary.wiley.com/doi/abs/10.1002/qj.49711750206>.
- R. J. Trapp. *Mesoscale-convective processes in the atmosphere*. Cambridge University Press, 2013.
- Z. Wang, J. A. Franke, Z. Luo, and E. J. Moyer. Reanalyses and a high-resolution model fail to capture the “high tail” of cape distributions. *Journal of Climate*, 34(21):8699 – 8715, 2021. doi: 10.1175/JCLI-D-20-0278.1. URL <https://journals.ametsoc.org/view/journals/clim/34/21/JCLI-D-20-0278.1.xml>.
- H. Wernli, M. Paulat, M. Hagen, and C. Frei. SAL—A Novel Quality Measure for the Verification of Quantitative Precipitation Forecasts. *Monthly Weather Review*, 136(11):4470–4487, Nov. 2008. ISSN 1520-0493, 0027-0644. doi: 10.1175/2008MWR2415.1. URL <https://journals.ametsoc.org/view/journals/mwre/136/11/2008mwr2415.1.xml>. Publisher: American Meteorological Society Section: Monthly Weather Review.
- H. Wernli, C. Hofmann, and M. Zimmer. Spatial Forecast Verification Methods Intercomparison Project: Application of the SAL Technique. *Weather and Forecasting*, 24(6):1472–1484, Dec. 2009. ISSN 1520-0434, 0882-8156. doi: 10.1175/2009WAF2222271.1. URL https://journals.ametsoc.org/view/journals/wefo/24/6/2009waf2222271_1.xml. Publisher: American Meteorological Society Section: Weather and Forecasting.
- C. Wong. Deepmind ai accurately forecasts weather — on a desktop computer. *Nature Briefing*, 2023. doi: 10.1038/d41586-023-03552-y.

7 Appendix A - Forecast scores of April 13, 06 UTC

Score	IFS	Pangu-Weather	GraphCast	FourCastNet
CAPE				
RMSE	330	304	*283	513
BIAS	-15	61	-17	* -8
FSS ₃₀₀	0.92	0.92	*0.96	0.92
FSS ₁₀₀₀	0.91	0.90	*0.92	0.81
S	-0.18	0.09	*0.03	-0.63
A	*0.03	0.1	-0.07	-0.05
L	0.02	0.03	*0.01	*0.01
DLS				
RMSE	4.6	4.2	*3.9	4.5
BIAS	-0.8	-0.5	-0.8	*-0.4
WMS				
RMSE	391	356	*296	383
BIAS	27	85	*-6	-27
FSS ₃₀₀	0.91	0.91	*0.95	0.91
FSS ₅₀₀	0.90	0.89	*0.93	0.88
S	*0.11	0.37	0.18	0.17
A	0.08	0.23	*-0.02	-0.08
L	0.04	0.05	*0.02	*0.02

Table 5: Forecast scores at 30h lead-time, best-performing model is marked in bold and with an asterisk

Score	IFS	Pangu-Weather	GraphCast	FourCastNet
CAPE				
RMSE	704	655	*470	574
BIAS	*3	273	-44	-200
FSS ₃₀₀	0.70	0.79	*0.84	0.74
FSS ₁₀₀₀	0.58	0.77	*0.81	0.55
S	-0.11	0.17	*0.08	-0.39
A	*0.02	0.45	-0.14	-0.64
L	0.14	*0.02	0.05	0.03
DLS				
RMSE	9.4	9.1	7.5	*6.5
BIAS	-1.7	*-1.2	-2.2	-1.5
WMS				
RMSE	592	610	*440	508
BIAS	-58	219	*-27	-154
FSS ₃₀₀	0.62	0.75	*0.82	0.69
FSS ₅₀₀	0.60	0.72	*0.80	0.67
S	*0.05	0.44	0.20	-0.21
A	-0.19	0.50	*-0.08	-0.61
L	0.14	*0.01	0.07	0.05

Table 6: Same as Table 5 but for 174h lead-time

8 Appendix B - CAPE and DLS forecasts for July 7, 2020, 06 UTC

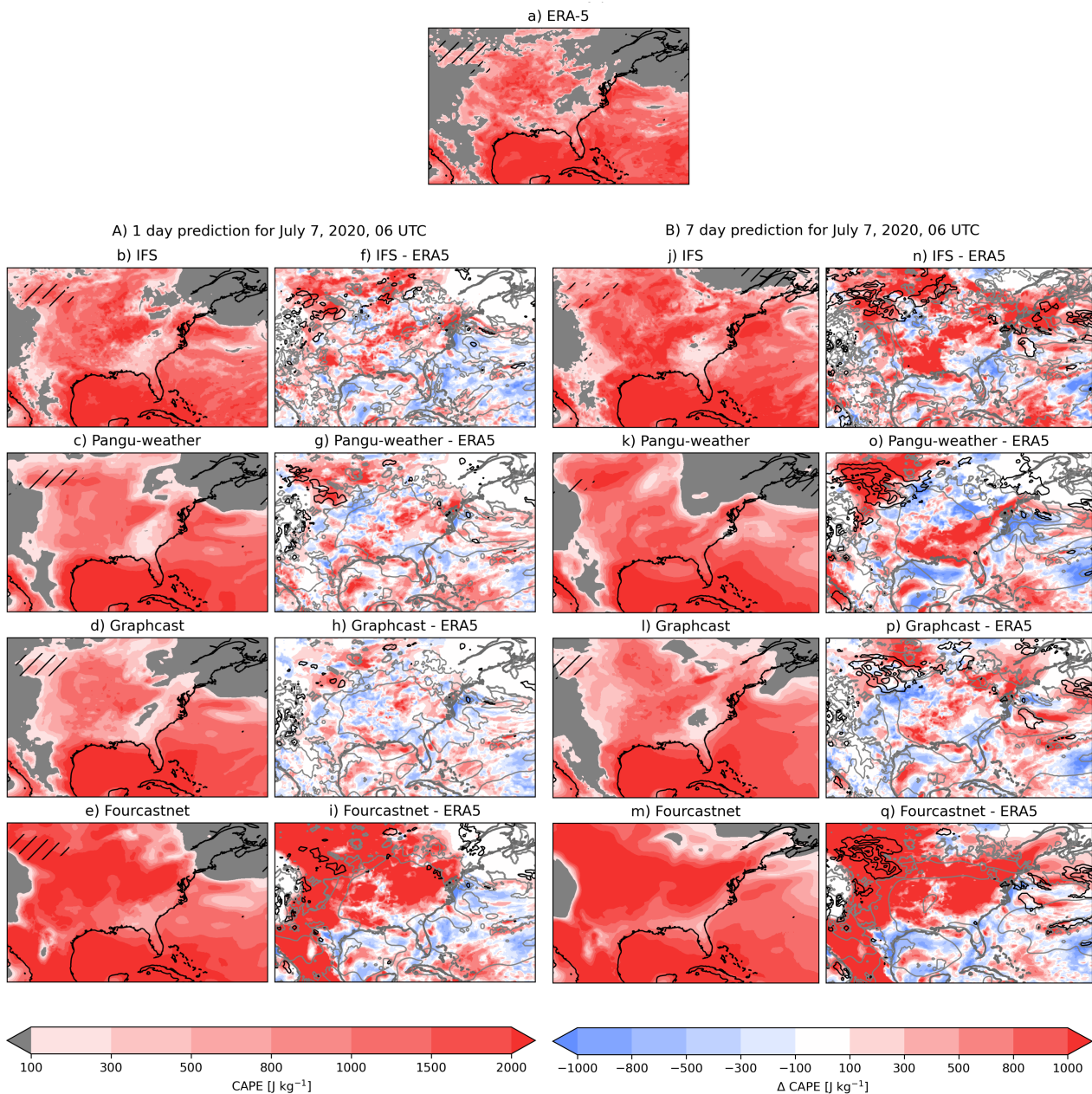


Figure 7: Comparison of forecasts of CAPE and DLS at 1 and 7 days lead-time; a) ERA-5 data of CAPE and DLS on July 7, 2020 at 06 UTC; A) 1 day forecast of CAPE and DLS (b-e) in comparison to ERA5 (f-i) B) 7 day forecast of CAPE and DLS (j-m) in comparison to ERA5 (n-q); hatched area indicates DLS $> 20 \text{ m s}^{-1}$; contours indicated positive (grey) and negative (black) areas of Δ DLS in 5 m s^{-1} increments